Energy Materials

Article

Defect-induced-reduced Au quantum Dots@MXene decorated separator enables lithium-sulfur batteries with high sulfur utilization

Yahao Du, Yuhong Liu, Feifei Cao[*], Huan Ye[*] iD

College of Chemistry, Huazhong Agricultural University, Wuhan 430070, Hubei, China.

*Correspondence to: Prof. Huan Ye, College of Chemistry, Huazhong Agricultural University, No. 1, Shizishan Street, Wuhan 430070, Hubei, China. E-mail: yehuan@mail.hzau.edu.cn; Prof. Feifei Cao, College of Chemistry, Huazhong Agricultural University, No. 1, Shizishan Street, Wuhan 430070, Hubei, China. E-mail: caofeifei@mail.hzau.edu.cn

Abstract

Although lithium-sulfur (Li-S) batteries have a high theoretical energy density, their practical applications are limited by rapid capacity fading and poor cycling stability due to the dissolution of high-order polysulfides in electrolytes and the sluggish kinetics of the solid-state Li_2S_2/Li_2S redox reaction. Herein, a polysulfide sorbent and redox reaction catalytic promoter, Au quantum dots (Au QDs)-decorated MXene nanosheet, is designed by proposing defect-induced-reduced $Ti_3C_2T_x$ (MXene) to improve the performance of Li-S batteries. The polar surface functional groups and high electronic conductivity of the MXene boost the conversion of sulfur/polysulfides and restrict the dissolution of the polysulfide shuttle. The Au QDs catalyst reduces the conversion reaction activation energy to achieve rapid solid-state Li_2S_2/Li_2S reaction kinetics. Due to the adsorption-catalysis synergistic effect between MXene and Au QDs, an initial discharge capacity of 1,500 mA h g^{-1} is obtained, corresponding to a sulfur utilization of 90%. A Li-S battery based on the Au QDs@MXene-decorated separator exhibits a capacity retention rate of 71.0% for 300 cycles at 1 C.

Keywords: Lithium-sulfur battery, separator, polysulfide, catalyst, high sulfur utilization

INTRODUCTION

Lithium-sulfur (Li-S) batteries have been considered as potential electrochemical energy storage systems due to their high theoretical energy density (2,600 Wh kg^{-1}), which is about seven times higher than that of LiCoO$_2$/graphite batteries (387 Wh kg^{-1})[1-3]. Moreover, sulfur is low-cost, eco-friendly, and naturally abundant. However, sulfur and its discharge products (Li$_2$S$_n$, $1 \le n \le 8$) show poor electronic and ionic conductivity, causing their batteries to exhibit large voltage polarization during galvanostatic discharge/ charge, ultimately resulting in capacity fading[4-7]. Insoluble sulfide reduction products (e.g., Li$_2$S$_2$ and Li$_2$S) that deposit on the pristine sulfur cathode can impede the reduction of interior sulfur particles, further reducing the sulfur utilization rate[8]. High-order lithium polysulfides (LiPSs) can react with the liquid electrolyte or dissolve in the electrolyte and produce a so-called shuttle effect that decreases the Coulombic efficiency and results in capacity loss[9,10]. High-order polysulfides can migrate to the Li anode and form an insoluble sulfide insulating layer driven by a concentration gradient, resulting in the loss of active sulfur and the growth of Li dendrites.

Numerous efforts have been devoted to developing advanced sulfur host materials to resolve the above issues[11-14]. Porous carbonaceous materials with high electronic conductivity and interconnected networks are widely used to alleviate the shuttle effect via the physical confinement of sulfur species[15-17]. However, due to the nonpolar surface of carbonaceous materials, they generally have a poor affinity for polar LiPSs, and the LiPSs will inevitably dissolve in the electrolyte during long-term cycling[18]. Hence, polar substrates that can strongly chemically adsorb LiPSs have been designed to accommodate sulfur particles[15,19-22]. However, capacity fading originating from the intrinsically sluggish reaction kinetics of the S/Li$_2$S reaction is not remedied by physical blocking and chemical adsorption. Based on this, catalysts have been applied to accelerate the conversion of LiPSs by reducing the reaction activation energy and thereby improving the sulfur utilization rate[23]. Various metal oxides, metal nitrides, sulfides, metal carbides, metal-organic frameworks (MOFs), their heterostructures, quantum dots (QDs), and signal atomic metals have been reported as catalysts[24-32]. Among them, QDs have attracted attention because of their quantum characteristics and edge effects. The nanoscale size (≤ 10 nm) of QDs gives them a high specific area that exposes sufficient active sites for LiPSs, thus improving the discharge capacity via the catalytic conversion of LiPSs[33]. However, QDs readily agglomerate into large particles due to their high surface energy, which weakens their catalytic activity. An efficient strategy to prevent QDs aggregation is to incorporate them in a 2D substrate. Transition-metal carbides and carbonitrides (MXenes) are promising 2D host materials due to their high electrical conductivity (10^4 S cm^{-1}) and strong LiPS adsorption ability[34-39]. Combining QDs and MXenes provides a heterostructure that suppresses the restacking of MXene and aggregation of QDs, thereby facilitating ion transport and sulfur dispersion. It also enhances the conductivity, which accelerates the reduction of sulfur.

In this context, an Au QDs-anchored MXene heterostructure (Au QDs@MXene) is engineered as a polysulfide adsorbent and redox reaction promoter via the defect-induced-reduction of MXene [Figure 1A]. MXenes with abundant polar surface functional groups show a strong affinity for sulfur, which prevents the shuttling of soluble LiPSs. The *in-situ* reduced Au QDs catalyst with high conductivity facilitates the rapid conversion between LiPSs and Li$_2$S$_2$/Li$_2$S by reducing the activation energy [Figure 1B]. This prevents the local gathering of LiPSs and improves the sulfur utilization rate. Due to the great adsorption-catalysis synergies of MXene and Au QDs, the Au QDs@MXene-decorated separator demonstrates a strong LiPS blocking ability and superior catalytic reaction kinetics, as evidenced by LiPS adsorption studies, X-ray photoelectron spectroscopy (XPS), and electrochemical analysis. The sulfur cathode based on the Au QDs@MXene-decorated separator delivers a high initial discharge capacity of 1,500 mA h g^{-1}, which is close to 90% of the theoretical specific capacity of sulfur. Moreover, the sulfur
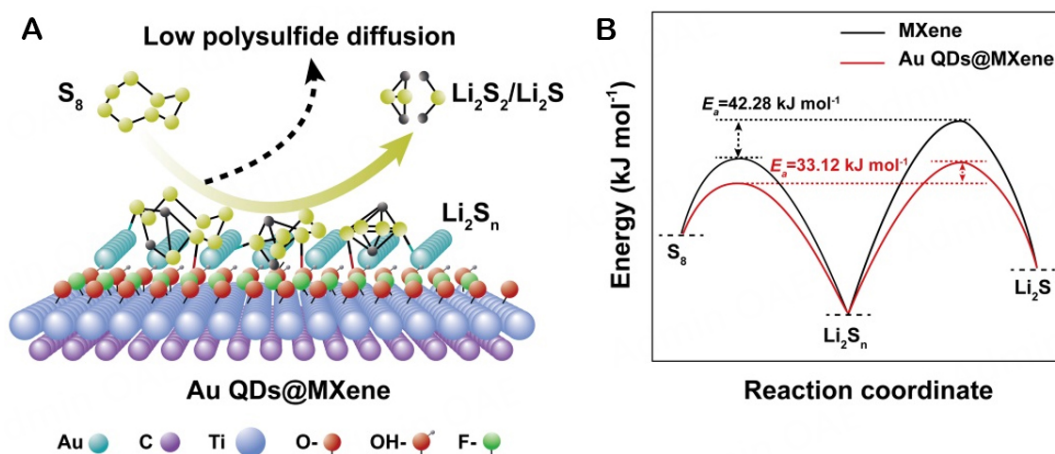
Figure 1. (A) Schematic of the conversion process of S/Li_2S on the Au QDs@MXene. (B) Activation energies of sulfur cathodes with different separators.

cathode paired with the Au QDs@MXene-decorated separator exhibits a capacity retention rate of 71.0% for 300 cycles at 1 C, indicating that Li-S batteries can be constructed by simply modifying the separator.

EXPERIMENTAL SECTION
Materials and reagents
The MAX (Ti_3AlC_2) was obtained from Jilin 11 Technology Co., Ltd. The ordered mesoporous carbon (abbreviated as CMK-3) with 3-4 nm-wide channel voids was bought from Nanjing XFNANO Materials Tech Co., Ltd. HCl was purchased from Sinopharm Chemical Reagent Co., Ltd. LiF ($\geq$ 99%) was obtained from Alfa Aesar (China) Chemical Co.Ltd. $HAuCl_4 \cdot 4H_2O$ was purchased from Tianjin MESco Chemical Co., Ltd. All the chemical reagents used in this work were of analytical grade.

Experimental procedures
Synthesis of $Ti_3C_2T_x$ nanosheets
1 g Ti_3AlC_2 powder was added in 9 mol/L HCl solution (20 mL) containing 1 g LiF at 25 °C for 24 h. The obtained mixture was centrifuged and washed with deionized water several times to remove impurities. Subsequently, the suspension was dispersed in deionized water through ultrasonic treatment to create a uniform solution. Finally, the solution was centrifuged to yield black $Ti_3C_2T_x$-MXene nanosheets with different sizes.

Synthesis of Au QDs@MXene nanosheets
Au QDs@MXene nanosheets were synthesized via an *in-situ* reduction method. Briefly, chlorauric acid solution (2 mM, $HAuCl_4 \cdot 4H_2O$) with different volumes was dropwise added to MXene solution (0.5 mg mL^{-1}) under ice bath condition to yield the Au QDs@MXene composites. The Au QDs@MXene composites were collected by centrifugation and dried in a vacuum oven at 40 °C for 12 h. The mass loading of Au QDs on the MXene nanosheets is 0.032 mg cm^{-2}.

Preparation of Au QDs@MXene-decorated separator
Au QDs@MXene powder, carbon black, and polyvinylidene fluoride (PVDF) at a mass ratio of 8:1:1 were ground thoroughly to form a uniform black slurry. Then, the slurry was cast on the surface of a Celgard separator. Following that, the Au QDs@MXene-decorated separator was dried in a vacuum oven at 40 °C for 24 h and cut into circular slices with a diameter of 19 mm with a microtome.

Fabrication of sulfur cathodes

Sulfur composite cathodes were prepared via a melt-molten method. Briefly, sulfur powder and CMK-3 at a mass ratio of 7:3 were uniformly mixed and then heated at 155 °C for 12 h. Afterward, the S cathode was prepared by mixing the CMK-3/S composite, Super P, and PVDF (Alfa Aesar) at a weight ratio of 8:1:1 with *N*-methyl-2-pyrrolidone (NMP, ≥ 99.5%, Sigma-Aldrich) as the solvent. The sulfur loading is about 2.5-5.1 mg cm^{-2}.

**Materials characterizations**

Scanning electron microscope (SEM, SU-8000, operating at 10 kV) and high-resolution transmission electron microscopy (HRTEM, JEOL-2100F) were used to characterize the morphology and surface structure of the as-obtained samples. The cross-section morphology of the samples was characterized using energy-dispersive X-ray spectroscopy (EDX, Bruker). X-ray diffraction (XRD) was accomplished on a Bruker D8 Advance diffractometer with Cu Kα radiation XRD (λ =1.54056 Å, 40 V, 30 mA) in the 2θ range of 5~80° to disclose the component of the materials. Ultraviolet-visible (UV-vis) absorption spectroscopy was measured in the 250-600 nm range to detect the content of polysulfides. An XPS (ESCALab 250Xi photoelectron spectrometer with Al Kα radiation) test was employed to study the surface composition and valence state of products.

Electrochemical tests

CR2032-type coin cells were assembled using a CMK-3/S composite cathode, an Au QDs@MXene-decorated polypropylene separator (PP, Celgard 2500, Goodfellow, USA), a Li foil anode, and a 1.0 M LiTFSI in 1,3-dioxolane (DOL)/1,2-dimethoxyethane (DME) (V/V = 1:1) electrolyte containing 2% LiNO$_3$. The electrochemical performances of batteries were evaluated using a LAND testing system. Electrochemical impedance spectra (EIS) measurements were conducted on a CHI-760E electrochemical workstation (CH Instruments Inc., Shanghai) with a frequency range from 0.1 Hz to 100 kHz. Cyclic voltammetry (CV) tests were performed on a CHI 760E electrochemical workstation at a scanning rate of 0.1 mV s^{-1}. Li$_2$S precipitation experiments are conducted to investigate the polysulfide conversion kinetics. A battery configuration based on Au QDs@MXene/MXene as the working electrode, Li foil as the counter electrode, and Li$_2$S$_8$ solution as the electrolyte, is applied to perform the Li$_2$S precipitation experiment. The cells are first galvanostatically discharged to 2.06 V to consume most soluble polysulfides and then potentiostatically held at 2.05 V until the current decreases to 10^{-5} A. The galvanostatic intermittent titration technique (GITT) of Li|Au QDs@MXene/PP|CMK-3/S| cells were performed at 0.1 C.

RESULTS AND DISCUSSION

The preparation scheme of Au QDs@MXene is presented in Figure 2A. First, a Ti$_3$C$_2$T$_x$ (MXene) heterostructure was prepared by selectively etching Al atom layers in bulk Ti$_3$AlC$_2$ according to a procedure reported in our previous work[40]. Then, as-obtained Ti$_3$C$_2$T$_x$ with abundant Ti vacancy defects showed strong reducibility, which facilitated the conversion of Au^{3+} to Au nanoparticles (Au NPs)[41]. *In-situ* generated Au NPs were distributed on Ti$_3$C$_2$T$_x$ sheets and formed Au QDs@MXene composites [Figure 2B]. The HRTEM images showed that the interplanar spacing was 0.271 nm for the heterostructure and 0.239 nm for the nanoparticles, which corresponded to the (0110) lattice plane of MXene and the (111) lattice plane of Au, respectively [Figure 2C and D][41]. The statistical size analysis of Au QDs@MXene showed that the average diameter of Au NPs ranged from 5 to 10 nm [Figure 2E]. X-ray powder diffraction (XRD) was used to characterize the composition of Au QDs@MXene. As shown in Figure 2F, only the characteristic peak of MXene was observed in the pattern of the composite material, which may be due to the low content and small size of NPs. The Au QDs@MXene heterostructure was plated on a commercial PP separator to fabricate a functional separator using a coating strategy. In Figure 2G, the Au QDs@MXene heterostructure tightly covered the PP separator with a coating thickness of around 7 μm. As a comparison,
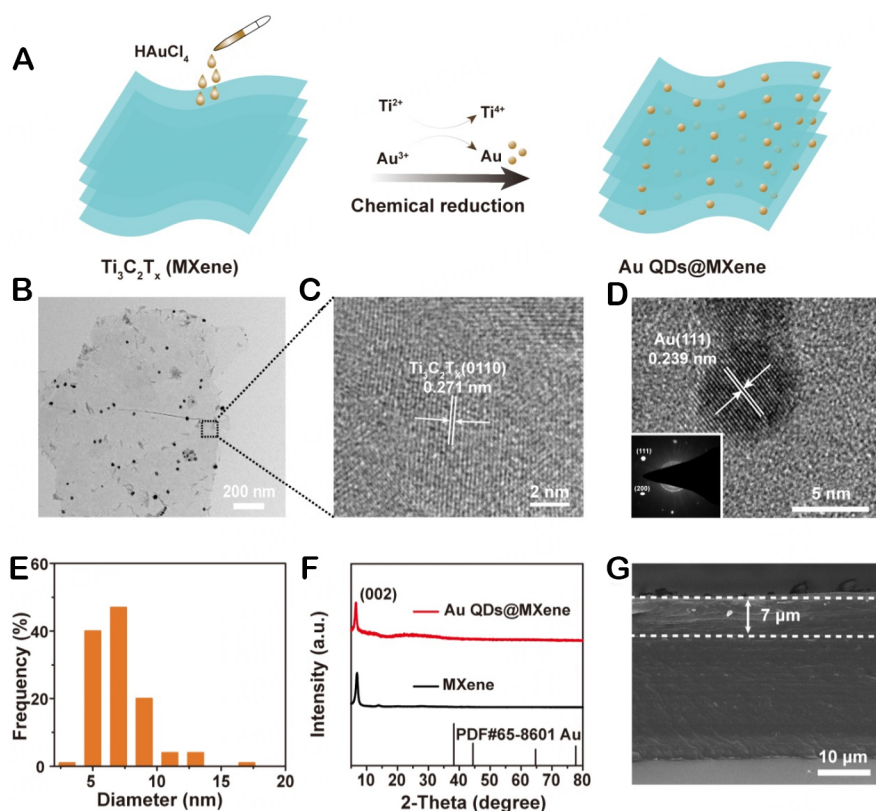
Figure 2. (A) Preparation scheme of Au QDs@MXene heterostructure. (B) TEM and (C and D) HRTEM images of Au QDs@MXene heterostructure. The inset is the selected area electron diffraction (SAED) pattern. (E) Grain size distribution of Au QDs. (F) XRD patterns of MXene and Au QDs@MXene heterostructure. (G) Cross-section SEM image of Au QDs@MXene-decorated separator.

the MXene-decorated separator with the same coating thickness was also prepared using the same scraping method [Supplementary Figure 1]. The bilayer structure of the separator is certified by the EDX elemental mappings through a good match in elemental mappings between Au, Ti, and O [Supplementary Figure 2]. The Au QDs@MXene-decorated PP separator was flexible and retained an intact structure without pulverization or cracking during repeated bending. This is necessary for long-term cycling stability when used in Li-S batteries [Supplementary Figure 3]. Thermal stability of the Au QDs@MXene-decorated PP separator is also characterized by a heating test. As shown in Supplementary Figure 4, an increase in temperature causes the PP separator to shrink and deform, potentially resulting in direct contact between the cathode and anode during cycling. This can ultimately lead to an internal short-circuit. In contrast, the Au QDs@MXene-modified separator maintains its structural integrity relatively well, showing minimal deformation even when subjected to a temperature of 170 °C. This is of significant importance for ensuring the safety of the battery. The wettability of liquid electrolytes toward the modified separator reflects the Li-ion transport speed, which can be confirmed by a contact angle test. Introducing the Au QDs@MXene nanosheets did not impede ionic transport, as shown by the slight decrease in the contact angle from 12.2 to 9.7° [Supplementary Figure 5].

The MXene heterostructure contains abundant surface functional groups that promote the adsorption of polar polysulfides, but these functional groups also increase the tendency to restack[34,42,43]. Au QDs with a large specific surface area prevented MXenes from restacking and provided adsorption sites. Permeation experiments were carried out to visually observe the penetration speed of polysulfides across different separators. As shown in Figure 3A, an H-bottle solution with Au QDs@MXene remained colorless after
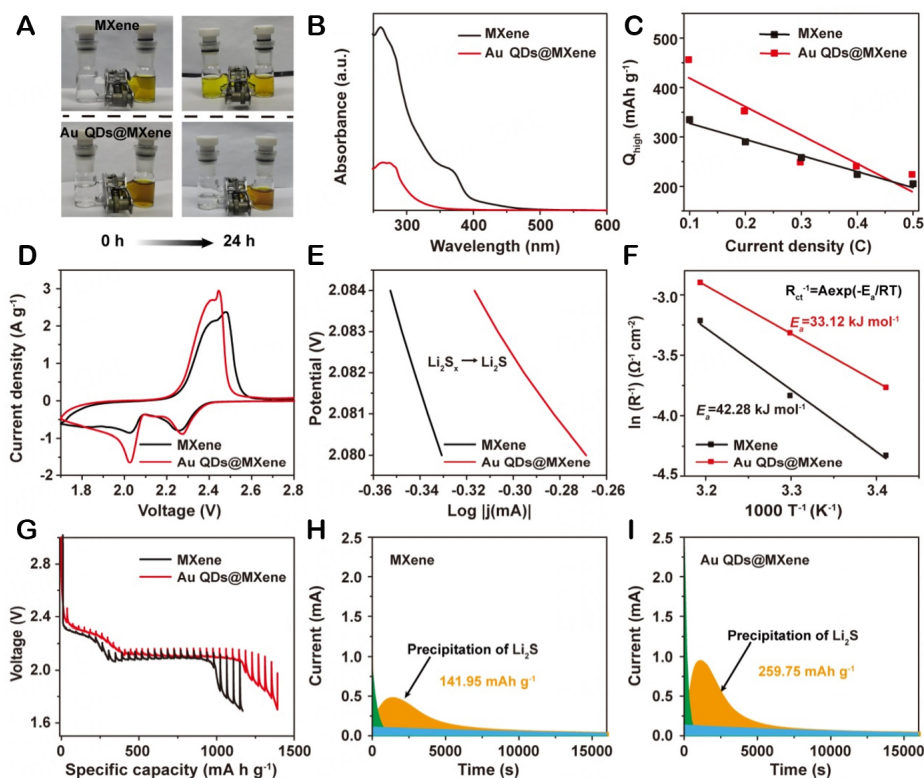
Figure 3. (A) Polysulfide permeation measurements for MXene-decorated and Au QDs@MXene-decorated separators during the course of polysulfides diffusion from the right side to the left side of the H-bottles. (B) UV-vis absorption spectra of Li_2S_6 solution on the left side of devices after 24 h. (C) Relationship between Q_{high} and current density of Li-S cells with the MXene-decorated and Au QDs@MXene-decorated separators. (D) CV curves of the MXene-based and Au QDs@MXene-based full cells at a scan rate of 0.1 mV s^{-1}. (E) Tafel plots corresponding to the reduction from Li_2S_x to Li_2S. (F) Activation energy profiles of different separators. (G) GITT curves of the discharge procedure. (H and I) Li_2S deposition profile of different samples.

static permeation for 24 h, while the control solution with MXene was bright yellow, indicating the superior polysulfide-blocking ability of Au QDs@MXene. After the permeation experiment, the polysulfide content on the left side of the H-bottle was analyzed using UV-vis spectroscopy. The Li_2S_6 absorbance with the Au QDs@MXene was remarkably lower than that with the MXene, further verifying that Au QDs@MXene provided superior polysulfide blocking [Figure 3B]. The shuttle constant (k_s) was used to evaluate the polysulfide shuttling behavior. The battery constructed using the Au QDs@MXene-decorated separator exhibited a higher slope than the battery with the MXene-decorated separator, indicating superior screening performance of Au QDs@MXene [Figure 3C].

Polar polysulfides must be strongly adsorbed for their subsequent rapid redox reactions on the catalyst. Hence, the role of the Au QDs@MXene in improving the redox reaction kinetics for S/Li_2S was explored by electrochemical analysis. As shown by the CV profiles [Figure 3D], the full cell based on the Au QDs@MXene-decorated separator exhibited a higher current response and narrower voltage separation than the full cell with the MXene-decorated separator. This indicates the higher reversibility of active S and the faster S/Li_2S conversion kinetics. The improved Li^+ transport ability was further confirmed by the lower interfacial resistance of the battery with the Au QDs@MXene-decorated separator than the battery with the MXene-decorated separator [Supplementary Figure 6]. The catalytic effect of Au QDs@MXene was further investigated by comparing the Tafel plots of the two cells with different separators. The Au QDs@MXene-based full cell showed a higher Tafel slope during both reduction and oxidation processes than those of the

MXene-based full cells. This indicates faster conversion from Li_2S_x to Li_2S [Figure 3E and Supplementary Figure 7].

The activation energies (E_a) were calculated from EIS spectra obtained at different temperatures, which reflect the S/Li_2S conversion rate [Supplementary Figure 8 and Supplementary Table 1]. As shown in Figure 3F, the E_a of the S/Li_2S conversion decreased by 9.16 kJ mol^{-1} for the Au QDs@MXene-based full cells compared with the MXene-based full cells. This implies that the S/Li_2S conversion rate was accelerated. The different conversion reaction kinetics for the two types of cells were compared using the GITT. The Au QDs@MXene-based full cells demonstrated higher discharge capacities and lower ohmic polarization and voltage polarization than the MXene-based full cells. This indicates the intrinsically faster charge transfer ability of the S cathode with the Au QDs@MXene-decorated separator [Figure 3G and Supplementary Figure 9]. The catalytic activity of Au QDs@MXene was also investigated by Li_2S precipitation experiments[44]. The Au QDs@MXene presented a shorter nucleation time (1,122.5 s) and Li_2S precipitation capacity (259.7 mA h g^{-1}) than MXene (1,450.9 s/141.9 mA h g^{-1}) [Figure 3H and I], confirming that Au QDs@MXene accelerated the kinetics of the redox reaction from Li_2S_x to Li_2S/Li_2S_2. The above results demonstrate the advantages of Au QDs@MXene in lowering the E_a and accelerating the redox kinetics of LiPSs.

To confirm the correlation between the Au NP size and catalytic activity, two other Au@MXene composites, referred to as Au NPs@MXene-1 and Au NPs@MXene-2, were prepared by regulating the chloroauric acid content using the same method [Supplementary Figures 10 and 11]. Upon increasing the Au NP size from 6 to 11 nm and further to 20 nm, E_a increased slightly from 33.12 kJ mol^{-1} to 34.94 kJ mol^{-1} and then to 36.79 kJ mol^{-1} [Supplementary Figure 12]. The Li-S battery with the smallest Au NPs (6 nm) exhibited the greatest discharge specific capacity and best capacity retention [Supplementary Figure 13]. The charge transfer resistance monotonically declined as the Au NP size decreased, indicating that the smallest Au NPs provided the fastest kinetics [Supplementary Figure 14]. The underlying reasons for the improved performances using smaller Au NPs were attributed to the increased number of exposed catalytically active sites[45]. Therefore, the separator anchored with 6 nm Au NPs was used to test its electrochemical properties in subsequent experiments.

The electrochemical performance of Li-S batteries using different modified separators was investigated. Due to the improved LiPS adsorption ability and catalytic activity, the Au QDs@MXene-based Li-S cells delivered a high initial discharge capacity of 1,500 mA h g^{-1}, corresponding to a high sulfur utilization rate of 90% at 0.2 C [Figure 4A]. After 100 cycles, the discharge capacity of the Au QDs@MXene-based full cell was maintained at 669 mA h g^{-1} [Figure 4B]. Even at a high rate of 0.5 C, the Au QDs@MXene-based full cell performed stably for 200 cycles and showed a capacity retention of 81% [Figure 4C]. The Au QDs@MXene also favored rapid Li^+/e^- transport, which ensured a superior rate capability. The reversible capacities obtained from the Li-S batteries based on the Au QDs@MXene-decorated separators were 1,150, 950, 830, 700, and 550 mA h g^{-1} at rates of 0.1, 0.3, 0.5, 1, and 2 C, respectively. These values are much higher than those obtained using the MXene-decorated separators [Figure 4D]. The superior LiPS screening performance and rapid sulfur redox reaction kinetics gave the Au QDs@MXene-based full cells long lifetimes and high-rate capabilities. The results of a long-term cycling test involving 300 charge/discharge cycles at 1 C are presented in Figure 4E. The Li-S battery with the Au QDs@MXene-decorated separator showed good cyclability and a capacity retention of 71% with a low decay rate of 0.092% during each cycle. Moreover, the cycling performance and rate of the high-sulfur-loaded sulfur cathodes are tested to highlight the advantages of Au QDs@MXene-decorated separators. As shown in Supplementary Figure 15, even when the sulfur loading is increased to twice the previous (approximately 5.1 mg cm^{-2}), the Li-S battery with the
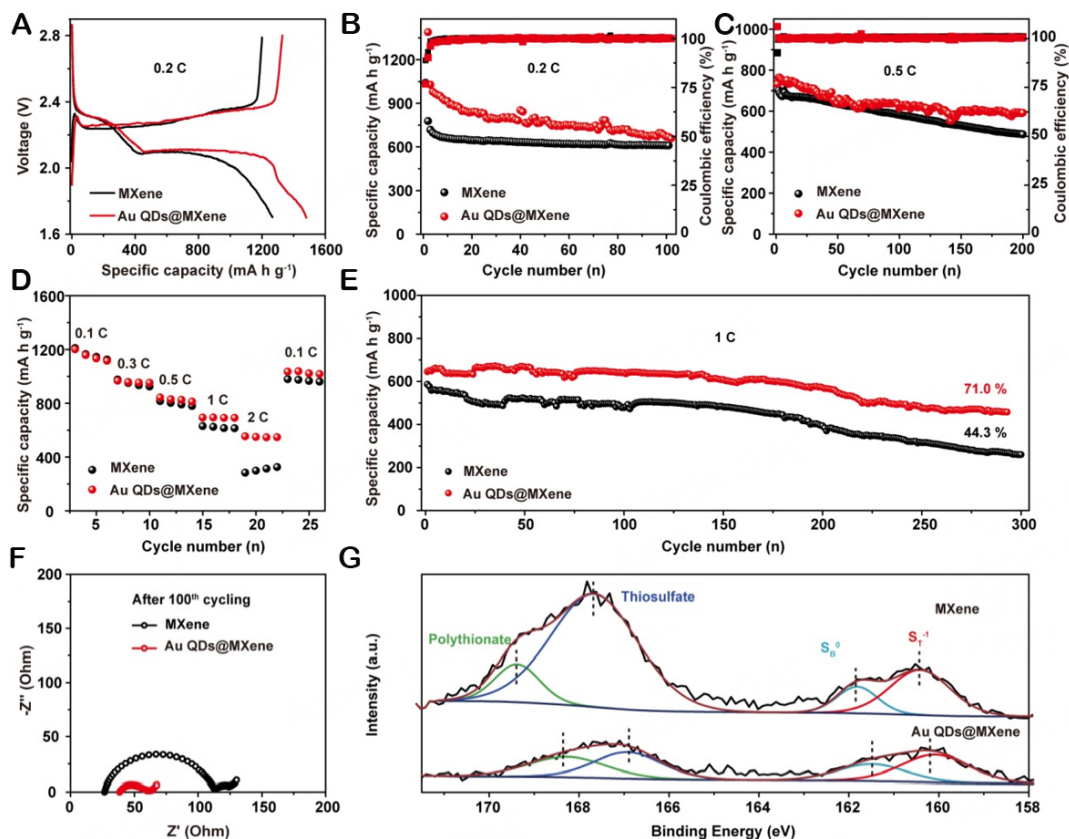
Figure 4. (A) Galvanostatic charge/discharge profiles of Li-S cells with MXene-decorated and Au QDs@MXene-decorated separators, and (B) corresponding cycling performance at 0.2 C (E/S ratio of 6.0 μL mg^{-1}). (C) Cycling performance comparison for the two cells at 0.5 C. (D) Rate performance of S cathodes with different separators. (E) Long-term cycling performance at 1 C. (F) EIS comparison of Li-S cells with MXene-decorated and Au QDs@MXene-decorated separators after the 100th cycle at 0.5 C. (G) XPS spectra of S 2p for the cycled Li anodes with MXene-decorated and Au QDs@MXene-decorated separators.

Au QDs@MXene-decorated separator still delivers a high initial discharge capacity of 1,091 mA h g^{-1}. The capacity is significantly higher than that of 838 mA h g^{-1} for the battery with the pure MXene-decorated separator. Furthermore, the battery with the Au QDs@MXene-decorated separator demonstrates good cycling performance, retaining 74% of its capacity after 50 cycles. In contrast, the pure MXene-decorated separator fails to achieve this level of performance [Supplementary Figure 15A]. Additionally, the rate capability of the battery with the Au QDs@MXene-decorated separator surpasses that of the battery with the pure MXene-decorated separator [Supplementary Figure 15B].

To further compare the effect of Au QDs@MXene versus bare MXene on the reaction kinetics and interfacial stability in batteries, we carried out EIS and *ex-situ* XPS. The first semicircle in the high-frequency region corresponded to Li$^+$ transfer via the interfacial layer on the S cathode and Li anode[15]. The interfacial resistance of the batteries with the Au QDs@MXene-decorated separator greatly decreased because of the rapid conversion of sulfur species and decreased accumulation of insulating Li$_2$S or Li$_2$S$_2$. The semicircle in the low-frequency region was related to the charge transfer resistance. The resistance of Au QDs@MXene was much lower than that of MXene, indicating the improved catalytic activity and electronic conductivity of the Au QDs@MXene-based batteries [Figure 4F]. XPS analysis was performed on the cycled Li anodes to investigate the shuttle effect. The spectra of both cells contained four peaks at 160.0, 161.4, 166.9, and 168.2 eV, which were attributed to the chemical bonds of S$_T^{-1}$, S$_B^0$, thiosulfate, and polythionate

[Figure 4G][46,47]. However, weaker sulfur peaks were observed from the Li surface with the Au QDs@MXene-decorated separator, indicating that polysulfides were converted to Li_2S on the cathode. This suppressed their migration toward the Li anode during cycling.

CONCLUSIONS AND OUTLOOK

In summary, we have realized the *in-situ* defect-induced preparation of Au QDs (~6 nm) that were evenly dispersed on an MXene as a functional separator for Li-S batteries. MXene, with a strong affinity for sulfur, chemically captured soluble polysulfides and suppressed their migration toward the Li anode. Au QDs with desirable electrocatalytic activity and high conductivity boosted the rapid conversion of polysulfides and reduced their local accumulation, thereby improving the sulfur utilization rate. Due to the strong chemisorption ability of MXene and the catalytic effect of Au QDs, the assembled Li-S batteries delivered a high reversible capacity of 1,500 mA h g^{-1} at 0.2 C, a favorable rate capability (cycled at 2 C), and exceptional long-term cycling (only 0.092% capacity fading per cycle over 300 cycles at 1 C). This concept of integrating chemisorption and catalysis provides a method to rationally design materials for Li-S (Se), Li-O_2, Na-S (Se), and Na-O_2 batteries.

DECLARATIONS

Authors' contributions

Conceived and designed the experiments, supervised the research, and provided funding and equipment: Ye H, Cao F

Writing - review and editing, figures set up: Du Y

Carried out the material preparation, characterization, and electrochemical analysis: Du Y, Liu Y

Supervised, edited, and revised the manuscript: Ye H

Availability of data and materials

The data supporting our work can be found in the Supplementary Materials.

Conflicts of interest

All authors declared that there are no conflicts of interest.

Ethical approval and consent to participate

Not applicable.

Consent for publication

Not applicable.

REFERENCES

1. Manthiram A, Chung SH, Zu C. Lithium-sulfur batteries: progress and prospects. *Adv Mater* 2015;27:1980-2006. DOI PubMed
2. Zheng ZJ, Ye H, Guo ZP. Recent progress in designing stable composite lithium anodes with improved wettability. *Adv Sci* 2020;7:2002212. DOI PubMed PMC
3. Zhao Y, Liu Z, Li Z, Peng Z, Yao X. Constructing stable lithium metal anodes using a lithium adsorbent with a high Mn^{3+}/Mn^{4+} ratio.

Energy Mater 2022;2:200034. DOI

4.   Zhou G, Chen H, Cui Y. Formulating energy density for designing practical lithium-sulfur batteries. *Nat Energy* 2022;7:312-9. DOI

5.   Yang CP, Yin YX, Ye H, Jiang KC, Zhang J, Guo YG. Insight into the effect of boron doping on sulfur/carbon cathode in lithium-sulfur batteries. *ACS Appl Mater Interfaces* 2014;6:8789-95. DOI

6.   Ye Z, Jiang Y, Li L, Wu F, Chen R. A high-efficiency CoSe electrocatalyst with hierarchical porous polyhedron nanoarchitecture for accelerating polysulfides conversion in Li-S batteries. *Adv Mater* 2020;32:e2002168. DOI

7.   Ren Y, Fan JS, Fu YZ. Recent strategies for improving the performances of rechargeable lithium batteries with sulfur- and oxygen-based conversion cathodes. *Energy Mater* 2023;3:300015. DOI

8.   Wang Z, Li Y, Ji H, Zhou J, Qian T, Yan C. Unity of opposites between soluble and insoluble lithium polysulfides in lithium-sulfur batteries. *Adv Mater* 2022;34:e2203699. DOI

9.   Ren W, Ma W, Zhang S, Tang B. Recent advances in shuttle effect inhibition for lithium sulfur batteries. *Energy Stor Mater* 2019;23:707-32. DOI

10. Guo W, Zhang W, Si Y, Wang D, Fu Y, Manthiram A. Artificial dual solid-electrolyte interfaces based on in situ organothiol transformation in lithium sulfur battery. *Nat Commun* 2021;12:3031. DOI PubMed PMC

11. Sun Z, Zhang J, Yin L, et al. Conductive porous vanadium nitride/graphene composite as chemical anchor of polysulfides for lithium-sulfur batteries. *Nat Commun* 2017;8:14627. DOI PubMed PMC

12. Li J, Chen C, Chen Y, et al. Polysulfide confinement and highly efficient conversion on hierarchical mesoporous carbon nanosheets for Li-S batteries. *Adv Energy Mater* 2019;9:1901935. DOI

13. Li Z, Xiao Z, Li P, Meng X, Wang R. Enhanced chemisorption and catalytic effects toward polysulfides by modulating hollow nanoarchitectures for long-life lithium-sulfur batteries. *Small* 2020;16:e1906114. DOI PubMed

14. Huang Y, Lin L, Zhang C, et al. Recent advances and strategies toward polysulfides shuttle inhibition for high-performance Li-S batteries. *Adv Sci* 2022;9:e2106004. DOI PubMed PMC

15. Peng HJ, Zhang G, Chen X, et al. Enhanced electrochemical kinetics on conductive polar mediators for lithium-sulfur batteries. *Angew Chem Int Ed* 2016;55:12990-5. DOI

16. Du Z, Guo C, Wang L, et al. Atom-thick interlayer made of CVD-grown graphene film on separator for advanced lithium-sulfur batteries. *ACS Appl Mater Interfaces* 2017;9:43696-703. DOI

17. Boyjoo Y, Shi H, Tian Q, et al. Engineering nanoreactors for metal-chalcogen batteries. *Energy Environ Sci* 2021;14:540-75. DOI

18. Wu F, Zhao S, Chen L, et al. Metal-organic frameworks composites threaded on the CNT knitted separator for suppressing the shuttle effect of lithium sulfur batteries. *Energy Stor Mater* 2018;14:383-91. DOI

19. Hua W, Li H, Pei C, et al. Selective catalysis remedies polysulfide shuttling in lithium-sulfur batteries. *Adv Mater* 2021;33:e2101006. DOI

20. Zhang M, Chen W, Xue L, et al. Adsorption-catalysis design in the lithium-sulfur battery. *Adv Energy Mater* 2020;10:1903008. DOI

21. Yao W, Tian C, Yang C, et al. P-doped $NiTe_2$ with Te-vacancies in lithium-sulfur batteries prevents shuttling and promotes polysulfide conversion. *Adv Mater* 2022;34:e2106370. DOI

22. Liu P, Qu L, Tian X, et al. $Ti_3C_2T_x$/graphene oxide free-standing membranes as modified separators for lithium-sulfur batteries with enhanced rate performance. *ACS Appl Energy Mater* 2020;3:2708-18. DOI

23. Shi Z, Ding Y, Zhang Q, Sun J. Electrocatalyst modulation toward bidirectional sulfur redox in Li-S batteries: from strategic probing to mechanistic understanding. *Adv Energy Mater* 2022;12:2201056. DOI

24. Liang Z, Shen J, Xu X, et al. Advances in the development of single-atom catalysts for high-energy-density lithium-sulfur batteries. *Adv Mater* 2022;34:e2200102. DOI

25. Zhang X, Yang T, Zhang Y, et al. Single zinc atom aggregates: synergetic interaction to boost fast polysulfide conversion in lithium-sulfur batteries. *Adv Mater* 2023;35:e2208470. DOI

26. He J, Bhargav A, Yaghoobnejad Asl H, Chen Y, Manthiram A. 1T′-ReS_2 nanosheets in situ grown on carbon nanotubes as a highly efficient polysulfide electrocatalyst for stable Li-S batteries. *Adv Energy Mater* 2020;10:2001017. DOI

27. Zhou G, Tian H, Jin Y, et al. Catalytic oxidation of Li_2S on the surface of metal sulfides for Li-S batteries. *Proc Natl Acad Sci USA* 2017;114:840-5. DOI PubMed PMC

28. Yang D, Liang Z, Tang P, et al. A high conductivity 1D π-d Conjugated metal-organic framework with efficient polysulfide trapping-diffusion-catalysis in lithium-sulfur batteries. *Adv Mater* 2022;34:e2108835. DOI

29. Ding Y, Cheng Q, Wu J, et al. Enhanced dual-directional sulfur redox via a biotemplated single-atomic Fe-N_2 mediator promises durable Li-S batteries. *Adv Mater* 2022;34:e2202256. DOI

30. Xiao Y, Xiang Y, Guo S, et al. An ultralight electroconductive metal-organic framework membrane for multistep catalytic conversion and molecular sieving in lithium-sulfur batteries. *Energy Stor Mater* 2022;51:882-9. DOI

31. Wang J, Ma Q, Sun S, et al. Highly aligned lithiophilic electrospun nanofiber membrane for the multiscale suppression of Li dendrite growth. *eScience* 2022;2:655-65. DOI

32. Shi H, Qin J, Lu P, et al. Interfacial engineering of bifunctional niobium (V)-based heterostructure nanosheet toward high efficiency lean-electrolyte lithium-sulfur full batteries. *Adv Funct Mater* 2021;31:2102314. DOI

33. Fujita T, Guan P, McKenna K, et al. Atomic origins of the high catalytic activity of nanoporous gold. *Nat Mater* 2012;11:775-80. DOI

34. Zhang C, Cui L, Abdolhosseinzadeh S, Heier J. Two-dimensional MXenes for lithium-sulfur batteries. *InfoMat* 2020;2:613-38. DOI

35. Li P, Lv H, Li Z, et al. The electrostatic attraction and catalytic effect enabled by ionic-covalent organic nanosheets on MXene for

separator modification of lithium-sulfur batteries. *Adv Mater* 2021;33:e2007803. DOI

36.   Lee DK, Chae Y, Yun H, Ahn CW, Lee JW. CO_2-oxidized $Ti_3C_2T_x$-MXenes components for lithium-sulfur batteries: suppressing the shuttle phenomenon through physical and chemical adsorption. *ACS Nano* 2020;14:9744-54. DOI

37.   Lei T, Chen W, Lv W, et al. Inhibiting polysulfide shuttling with a graphene composite separator for highly robust lithium-sulfur batteries. *Joule* 2018;2:2091-104. DOI

38.   Gu S, Jiang H, Li X, et al. Dispersing single-layered $Ti_3C_2T_x$ nanosheets in hierarchically-porous membrane for high-efficiency Li^+ transporting and polysulfide anchoring in Li-S batteries. *Energy Stor Mater* 2022;53:32-41. DOI

39.   Zhang Y, Ma C, He W, et al. MXene and MXene-based materials for lithium-sulfur batteries. *Prog Nat Sci Mater Int* 2021;31:501-13. DOI

40.   Liu YH, Wang CY, Yang SL, Cao FF, Ye H. 3D MXene architectures as sulfur hosts for high-performance lithium-sulfur batteries. *J Energy Chem* 2022;66:429-39. DOI

41.   Liu C, Zhang H, Li R, et al. Laser triggered exothermic chemical reaction in Au nanoparticle@Ti_3C_2 MXene membrane: a route toward efficient light to high-temperature pulse conversion. *Chem Eng J* 2021;420:127672. DOI

42.   Xiong D, Huang S, Fang D, et al. Porosity engineering of MXene membrane towards polysulfide inhibition and fast lithium ion transportation for lithium-sulfur batteries. *Small* 2021;17:e2007442. DOI

43.   Yang C, Li Y, Peng W, Zhang F, Fan X. In situ N-doped CoS_2 anchored on MXene toward an efficient bifunctional catalyst for enhanced lithium-sulfur batteries. *Chem Eng J* 2022;427:131792. DOI

44.   Fan FY, Carter WC, Chiang YM. Mechanism and kinetics of Li_2S precipitation in lithium-sulfur batteries. *Adv Mater* 2015;27:5203-9. DOI PubMed

45.   Lang X, Hirata A, Fujita T, Chen M. Nanoporous metal/oxide hybrid electrodes for electrochemical supercapacitors. *Nat Nanotechnol* 2011;6:232-6. DOI PubMed

46.   Yao WQ, Zheng WZ, Xu J, et al. ZnS-SnS@NC Heterostructure as robust lithiophilicity and sulfiphilicity mediator toward high-rate and long-life lithium-sulfur batteries. *ACS Nano* 2021;15:7114-30. DOI

47.   He JR, Luo L, Chen YF, Manthiram A. Yolk-shelled C@Fe_3O_4 nanoboxes as efficient sulfur hosts for high-performance lithium-sulfur batteries. *Adv Mater* 2017;29:1702707. DOI